Research Paper

Segmentation of Aggregate and Asphalt in Photographic Images of Pavements

Angela Marcela MEJÍA[1)*], Marco Aurelio ALZATE[2)],
Oscar Javier REYES-ORTIZ[1)]

[1)] *School of Engineering, Universidad Militar Nueva Granada*
Bogotá, Colombia; e-mail: oscar.reyes@unimilitar.edu.co
[*]Corresponding Author e-mail: angela.mejia@unimilitar.edu.co

[2)] *School of Engineering, District University of Bogotá*
Bogotá, Colombia
e-mail: malzate@udistrital.edu.co

Particle size distribution of aggregate in asphalt pavements is used for determining important characteristics like stiffness, durability, fatigue resistance, etc. Unfortunately, measuring this distribution requires a sieving process that cannot be done directly on the already mixed pavement. The use of digital image processing could facilitate this measurement, for which it is important to classify aggregate from asphalt in the image. This classification is difficult even for humans and much more for classical image segmentation algorithms. In this paper, an expert committee approach was used, including classical adaptive Otsu, k-means vector quantization over a set of 8 principal components obtained from 26 features, and a Gaussian mixture model whose parameters are estimated through the expectation-maximization algorithm. A novel cellular automata approach is used to coordinate these expert opinions. Finally, a simple heuristic is used to reduce sub- and over-segmentation. The segmentation results are comparable to those obtained by a human expert, while the sieve size of the segmented images corresponds very well with that obtained from the sieving process, validating the proposed method of segmentation. The results show that with the digital imaging procedure it was possible to detect particles with a size of 100 μm with 90% of success with respect to time-consuming manual techniques. In addition, with these results it is possible to establish the homogeneity of the sample and the distribution of the particles within the asphalt mixture.

Key words: image segmentation; Gaussian mixture model; cellular automata; asphalt pavement; sieve size.

1. Introduction

Road infrastructure is an important support for the social and economic development of a country because it is used for the exchange of goods, the mobility

of people and the interaction between regions [1]. However, the investment and the financial cost of building such infrastructure are high. For this reason, the study, maintenance and construction of economically and environmentally sustainable, durable and efficient roads are essential for the economy of a country [2].

Laboratory tests are traditionally carried out for the study and quality control of the construction of the pavements. Samples of asphalt mixtures are tested using different methodologies to establish their sieve size, asphalt content, maximum load, deformation, ductility and modulus, among other mechanical and dynamic properties [3]. There are several problems presented by this type of tests that limit its use: they are mostly destructive tests that generate a high cost, they take long periods of time, and they require costly and specialized equipment, not accessible to many research centers [4].

Trends in new technologies such as digital image processing, computational modeling, artificial intelligence and the application of finite elements, have been shown to be versatile tools that can be used in this area economically, quickly and non-destructively [5]. Digital image processing, in particular, has been used in fields like medicine, agriculture, geology and civil engineering for characterizing the components of a mixture where internal particles affect directly their behavior [6, 7].

Unfortunately, it is not easy to identify, count and measure aggregate particles in a digital image of pavement, either because they are not clearly separated or because they are partially buried in asphalt. Furthermore, images are noisy, aggregate has irregular shape, some characteristics of asphalt are present within several aggregate, there are many differences among aggregate, etc.

For classification of pixels as aggregate or asphalt, humans use such characteristics as color, texture, shape, brightness, etc., but there are situations where classification is difficult even for us.

After testing several alternatives, we decided to use a cellular automata approach to combine the opinion of three experts: adaptive Otsu, 8-dim vector quantization, and a parametric probabilistic model. The results are comparable to those obtained by humans. Furthermore, the results of gradation test analysis are comparable to those obtained through sieving procedures.

Next section describes some previous work in this area while Sec. 3 describes the mathematical model of the pavement image. Subsection 3.1 is a presentation of the main image processing procedures used in this work, including adaptive Otsu thresholding, feature selection, principal components analysis, adaptive vector quantization over eight principal components and a Gaussian Mixture Model estimated through the expectation/maximization algorithm. Each of these techniques leads to interesting results that are exploited in an experts committee, where two cellular automata followed by a region growing procedure solve for differences on experts opinions, as explained in Subsec. 3.2. Section 4 shows the

particle size and gradation analysis on the segmented images and Sec. 5 concludes the paper.

2. Previous work

Some previous works in the field of pavement engineering include the evaluation and detection of the aggregate distribution of an asphalt mixture using X-rays, taking into account the coarse aggregate by dividing the sample into regions with no regard of individual particles [8]. Other methods are based on computer tomography to reconstruct three-dimensional models of asphalt mixtures seeking to characterize the particles and estimate their properties [9]. More specifically, digital image processing has been used for the analysis of the aggregate in recycled concrete to determine the amount of mortar adhered to the aggregates of higher size [10]. This type of works provides low-cost, non-destructive and fast tools for the analysis of sieve size and show a great efficiency for the detection of the affected areas. In this section, we briefly review some of these works.

Image segmentation and classification are two of the most studied digital image processing applications [11]. There are many ingenious methods to segment images ranging from simple histogram and thresholding methods like Otsu's [12], going through several edge detection algorithms [13], morphological watersheds [14] and region growing, splitting and merging [15], to probabilistic models and computational intelligence methods [16]. The proliferation of such number of alternatives means, among other things, that image segmentation and classification is, normally, a difficult task.

Nevertheless, digital image processing has been used recently as a plausible method for different purposes in asphalt pavements research. As early as 1996, digital image processing techniques have been applied to quantify the distribution, orientation, and shape of coarse aggregates in asphalt/concrete mixtures [17]. Morphological image processing techniques have been used to estimate the angularity of 3-dimensional particles in particulate materials [18]. X-ray computed tomography images have been used with automated digital image algorithms for processing asphalt concrete [19–21]. The effect of adding aggregates with different Nominal Maximum Aggregate Size on the microstructure of asphalt mixtures using images of asphalt mixture is studied in [22]. Images captured during the fall of particles at production stages are studied in [23]. Mixture microstructure is identified in [24] using connected-component labeling algorithm on a color photo of a soil and rock mixture. An interesting review of image processing for failure detection in pavements is carried out in [25]. In [26], image segmentation into gravel and asphalt classes is used to construct a model of the micromechanical properties of the mixture. An imaging standard for asphalt

mixtures is reported in [27]. University of Wisconsin at Madison and Michigan State University have developed iPas, a software in Matlab implementing the techniques in this standard, including contrast enhancement through histogram equalization, median filtering for noise reduction, two-threshold binarization, edge-detection, image segmentation by Canny operator and watershed correction through morphological operators [28]. However, this is not really an automatic system since it requires an interactive help from the user. The authors of [29] recorded images of fractures in order to assess the dependence of asphalt mixtures' fracture response on loading rate, temperature, and recycled content. In [30], an interesting similar process is reported. In [31], Digital Imaging Processing and spectral analysis are combined to quantify the superficial removal of bitumen and the exposure of aggregates. An elaborate method of characterization of internal asphalt microstructure based on the skeleton of a digital image is reported in [32].

In all previous works, the problem of segmentation of simple photographic images of pavement is not the most important one, so the problem is poorly treated or completely omitted. Digital image processing techniques are reduced to texture analysis, or are applied to elaborate X-Ray tomographic images, or based on manually configured parameters. In this paper, we design a completely automatic segmentation algorithm and evaluate it for sieve size purposes. As described in the rest of this paper, we use a cellular automata approach to combine the partial results of an adaptive Otsu method, an 8-dim vector quantization technique and a parametric probabilistic model. The segmentation results are comparable to those obtained by humans and the gradation test results are comparable to those obtained through the sieving procedures.

3. Materials and methods

Let $\mathbb{Z}_N$ be the set of integers between zero and $N-1$, $\mathbb{Z}_N = \{0, 1, 2, ..., N-1\}$. An image is an array of $N_V \times N_H$ pixels, where N_V is the number of rows and N_H is the number of columns. This is, an image is a function with domain $\mathbb{Z}_{NV} \times \mathbb{Z}_{NH}$. Each element of the array (each pixel) can take a particular value in a discrete set. For example, the color image obtained from the camera, I_c, is a function from $\mathbb{Z}_{NV} \times \mathbb{Z}_{NH}$ to $\mathbb{Z}_L \times \mathbb{Z}_L \times \mathbb{Z}_L$, where the value that each pixel can take is a 3-dimension vector $[R, G, B]^{\mathrm{T}}$, where R, G, and B are integers between 0 and $L - 1$ representing the red, green, and blue levels, respectively:

$$(3.1) \qquad I_C : \mathbb{Z}_{N_V} \times \mathbb{Z}_{N_H} \to \mathbb{Z}_L \times \mathbb{Z}_L \times \mathbb{Z}_L.$$

Usually, the number of levels for each color in a pixel is $L = 256$, represented with eight bits, for a total of 24 bits per pixel. Color information can be omitted

to use only the corresponding intensity value, also called luminosity or gray level, which reduces the co-domain to the set $\mathbb{Z}_L$:

$$(3.2) \qquad I_G : \mathbb{Z}_{N_V} \times \mathbb{Z}_{N_H} \to \mathbb{Z}_L,$$

where a pixel with a zero value is black, a pixel with a value $L-1$ is white and other values correspond to intermediate gray levels between black and white. The fundamental idea in this paper is to achieve a transformation of the I_C and I_G images into a new I_S image in the same domain of I_C and I_G but with co-domain $\mathbb{Z}_2 = \{0,1\}$, where the pixels in zero state correspond to asphalt and the pixels in state 1 correspond to gravel:

$$(3.3) \qquad I_S : \mathbb{Z}_{N_V} \times \mathbb{Z}_{N_H} \to \mathbb{Z}_2 = \{0,1\}.$$

If $\mathscr{I}_C$ is the set of all possible photographs of pavement samples with $N_V \times N_H$ pixels and $\mathscr{I}_S$ is the set of all possible binary images with $N_V \times N_H$ pixels, we want to find a transformation

$$(3.4) \qquad T : \mathscr{I}_C \to \mathscr{I}_S$$

such that $I_S = T(I_C)$ corresponds to the correct selection of gravel and asphalt elements in the original I_C image, for any $I_C \in \mathscr{I}_C$. Figure 1 shows an example of an I_C image with its corresponding I_G and I_S images, where I_S was obtained manually.
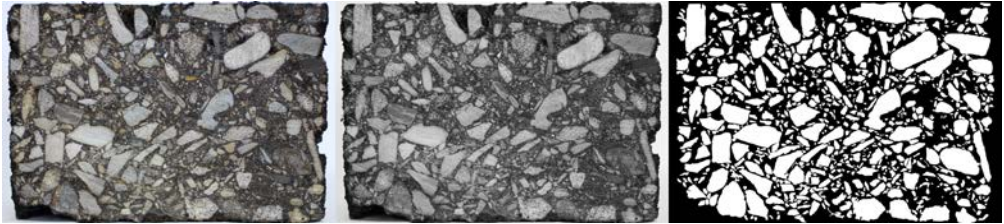

FIG. 1. Example of an I_C color image and its corresponding gray and binary versions, I_G and I_S.

The object to be photographed is a cylindrical asphalt sample with an average diameter size of 10 cm and height between 6.35 at 7.05 cm (average 6.7 cm). With an industrial cutter the specimen is cut diametrically. The image is captured in a space with white illumination and the object is located 30 cm from the capture device.

It is interesting to notice that the images are taken under natural light, since possible uneven brightness and uncertain light direction are compensated during the image processing stages.

3.1. *Image processing*

All the images have a light border around the asphalt mixture, which, in the gray version in $\mathbb{Z}_{256}$, always has an intensity greater than 90. For this reason, the light border can be easily removed by comparing the levels of gray with 90, filling in the gaps, calculating the convex hull of the selected area and choosing the maximum rectangle contained in said convex hull, as shown in Fig. 2.
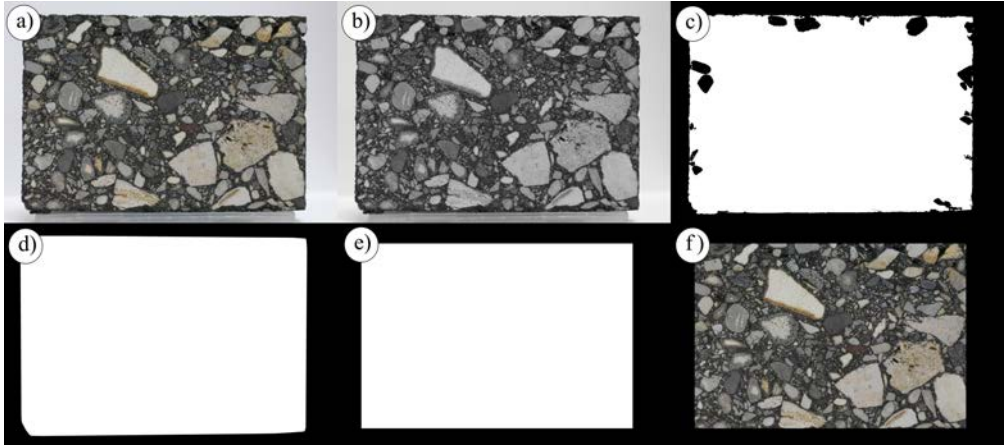

FIG. 2. Border elimination. Clockwise from upper left: (a) original image, (b) gray image, (c) filled region with intensity less than 90, (d) convex hull, (e) maximum rectangle contained in the convex hull, (f) final image to process.

The convex hull of Fig. 2d has N_{CH} pixels representing an area of 10×6.7 cm^2. Consequently, the surface resolution of the image is $ppsc = N_{CH}/67$ pixels per square centimeter. Thus, to calculate the area in cm^2 of any region that has N_P pixels we use the relation $Area = N_P/ppsc$, i.e.,

$$(3.5) \qquad\qquad Area(N_P) = 67\frac{N_P}{N_{CH}} \ [\text{cm}^2].$$

Before attempting any segmentation process, the image (either I_C or I_G) is passed through an adaptive histogram equalizer [34] to improve the contrast between pixels, and through a median filter to reduce the noise without affecting the edges [35]. The parameters of the adaptive equalization are chosen in order to emphasize the small dark aggregate without too much emphasis on the textures within the aggregate, which could make the classification more difficult.

One of the simplest and most effective segmentation methods is based on noting that most pixels corresponding to aggregate are light and most pixels corresponding to asphalt are dark. The method uses a comparison level l_0 to

binarize the I_G image so that the pixels whose intensity is greater than or equal to l_0 are classified as aggregate and other pixels are classified as asphalt:

$$(3.6) \qquad I_S(x,y) = \begin{cases} 0 & \text{if } I_G(x,y) < l_0, \\ 1 & \text{if } I_G(x,y) \geq l_0, \end{cases} \qquad \forall (x,y) \in \mathbb{Z}_{N_V} \times \mathbb{Z}_{N_H}.$$

The comparison level is chosen according to different criteria such as the maximization of the variance between classes (or minimization of the variance within each class), or Otsu method [36]. After classifying each pixel, a hole filling process is done to erase the dark elements within the aggregate regions.

Processing $I_G(x,y)$ with this method, we can get good results in some homogeneous regions of the image and discouraging results in some non-homogeneous regions (where different aggregates overlap in a single region or a single aggregate is separated in different regions). These difficulties will be the ones we deal with in this paper.

Indeed, some gravel are dark relative to the whole image but slightly lighter than its surrounding asphalt. Detecting this aggregate requires a low threshold. On the other hand, some borders between adjacent bright aggregates, which should be classified as asphalt, are lighter than many dark aggregate. Detecting this asphalt requires a high threshold. This is why a single threshold Otsu's method is inappropriate, so we better use an adaptive version where the whole image is divided in 16×16 subimages, each of them segmented independently through Otsu. Figure 3 shows the results.
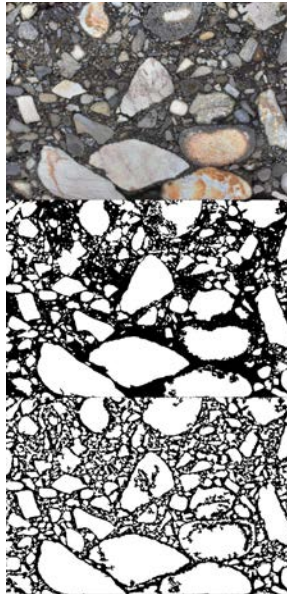

FIG. 3. Otsu and adaptive Otsu in asphalt/aggregate segmentation.

Although we have got much better results with adaptive Otsu method, the two mentioned difficulties persist, so we will use more information than the simple individual gray level of each pixel. It can be shown that the Otsu method is equivalent to a vector quantization approach based on the 2-means method [37]. However, the 2-means method can be used not only on the one-dimensional space of the gray intensities but on multidimensional vectors with more general characteristics of each pixel. We will use information that reflects brightness and color of each pixel as well as brightness and texture of its neighborhoods at different scales, since these seems to be the elements that we humans use to distinguish aggregate from asphalt [38]. In particular, we will consider the following $M = 26$ characteristics:

(1) Gray level: this is simply the value of the pixel in I_G

$$(3.7) \qquad d_1(x, y) = I_G(x, y), \qquad (x, y) \in \mathbb{Z}_{N_V} \times \mathbb{Z}_{N_H}.$$

(2) Hue: we consider the RGB values of each pixel in I_C and the minimum of the values among these spectral bands,

$$mn(x, y) = \min \left\{ R(x, y), G(x, y), B(x, y) \right\}, \qquad (x, y) \in \mathbb{Z}_{N_V} \times \mathbb{Z}_{N_H},$$

to compute the hue as follows:

$$(3.8) \qquad d_2(x, y) = \sqrt{a^* + b^* + c^*}, \qquad (x, y) \in \mathbb{Z}_{N_V} \times \mathbb{Z}_{N_H},$$

where

$$a^* = (R(x, y) - mn(x, y))^2, \quad b^* = (G(x, y) - mn(x, y))^2,$$

$$c^* = (B(x, y) - mn(x, y))^2.$$

A pixel with zero hue has $R = G = B$, so it is in the gray scale, regardless of whether it is black, white or any intermediate gray. A purely yellow, purely magenta or purely cyan pixel of maximum luminosity has the maximum hue value, $(L - 1)\sqrt{2}$. A purely red, purely green or purely blue pixel of maximum luminosity has a hue value of $L - 1$.

(3) The average value of gray levels in a 5×5 neighborhood around the pixel

$$(3.9) \qquad d_3(x, y) = \frac{1}{25} \sum_{j=-2}^{2} \sum_{k=-2}^{2} I_G(x + j, y + k).$$

The importance of this parameter is that, although the luminosity of the pixel is perhaps the most discriminating parameter, it is also important to know if the pixel is within a light or dark region.

(4) The entropy of gray levels in a 5×5 neighborhood around the pixel. A list of the different gray values in the neighborhood is computed as well as the relative frequency of each gray level in the list, p_i. The normalized relative frequency is used to compute the Shannon entropy

$$(3.10) \quad d_4(x, y) = -\sum_{i=0}^{L} p_i(x, y) \log_2 (p_i(x, y)), \quad (x, y) \in \mathbb{Z}_{N_V} \times \mathbb{Z}_{N_H},$$

where

$$(3.11) \quad p_i(x, y) = \frac{1}{25} \sum_{j=-2}^{2} \sum_{k=-2}^{2} \mathbf{1} \left(I_G(x + j, y + k) = i\right) \bigg|_{i \in \mathbb{Z}_L},$$

and $\mathbf{1}(A)$ is the indicator function of proposition A, which is 1 if A is true and is 0 if A is false. This way, $p_i(x, y)$ becomes the probability of the i-th gray level within the 25 pixels of the neighborhood. If all 25 pixels are different, the entropy is maximum ($\log_2(25) = 4.6439$ bits). If all 25 pixels have the same value, the entropy is minimum (0 bits). Entropy is a preliminary measure of texture in the image in the sense that a low-variable image has a low entropy and a highly variable image has a high entropy. The following two measurements complement the description of the texture around the pixel.

(5) The range of gray levels in a 5×5 neighborhood around the pixel

$$(3.12) \quad d_5(x, y) = d^* - e^*, \quad (x, y) \in \mathbb{Z}_{N_V} \times \mathbb{Z}_{N_H},$$

where

$$d^* = \max_{i,j \in \{-2,-1,0,1,2\}} I_G(x + i, y + j).$$

$$e^* = \min_{i,j \in \{-2,-1,0,1,2\}} I_G(x + i, y + j).$$

While entropy only considers the number of different values, the range considers the differences among those values.

(6) The standard deviation among gray levels in a 5×5 neighborhood around the pixel

$$(3.13) \quad d_6(x, y) = \sqrt{\frac{1}{25} \sum_{j=-2}^{2} \sum_{k=-2}^{2} \left(I_G(x + j, y + k) - d_3(x, y)\right)^2}.$$

Consider a neighborhood that has all its pixels at zero except for a pixel that has a gray level of 255. That neighborhood has the same rank as a neighborhood with 25 different gray values between 0 and 255, but the standard deviation is smaller.

(7) $d_7(x, y)$ is the average value of gray levels in a 9×9 neighborhood around the pixel.

(8) $d_8(x, y)$ is the entropy of gray levels in a 9×9 neighborhood around the pixel.

(9) $d_9(x, y)$ is the range of gray levels in a 9×9 neighborhood around the pixel.

(10) $d_{10}(x, y)$ is the standard deviation among gray levels in a 9×9 neighborhood around the pixel.

(11) $d_{11}(x, y)$ is the average value of gray levels in a 17×17 neighborhood around the pixel.

(12) $d_{12}(x, y)$ is the entropy of gray levels in a 17×17 neighborhood around the pixel.

(13) $d_{13}(x, y)$ is the range of gray levels in a 17×17 neighborhood around the pixel.

(14) $d_{14}(x, y)$ is the standard deviation among gray levels in a 1×17 neighborhood around the pixel.

(15) $d_{15}(x, y)$ is the average value of gray levels in a 33×33 neighborhood around the pixel.

(16) $d_{16}(x, y)$ is the entropy of gray levels in a 33×33 neighborhood around the pixel.

(17) $d_{17}(x, y)$ is the range of gray levels in a 33×33 neighborhood around the pixel.

(18) $d_{18}(x, y)$ is the standard deviation among gray levels in a 33×33 neighborhood around the pixel.

(19) $d_{19}(x, y)$ is the average value of gray levels in a 65×65 neighborhood around the pixel.

(20) $d_{20}(x, y)$ is the entropy of gray levels in a 65×65 neighborhood around the pixel.

(21) $d_{21}(x, y)$ is the range of gray levels in a 65×65 neighborhood around the pixel.

(22) $d_{22}(x, y)$ is the standard deviation among gray levels in a 65×65 neighborhood around the pixel.

(23) $d_{23}(x, y)$ is the average value of gray levels in a 129×129 neighborhood around the pixel.

(24) $d_{24}(x, y)$ is the entropy of gray levels in a 129×129 neighborhood around the pixel.

(25) $d_{25}(x, y)$ is the range of gray levels in a 129×129 neighborhood around the pixel.

(26) $d_{26}(x, y)$ is the standard deviation among gray levels in a 129×129 neighborhood around the pixel.

All this data is taken after the equalization and the median filters. Finally, all data is normalized in the interval $[0, 1]$. Figure 4 shows the $M = 26$ different characteristics measured on a particular image.
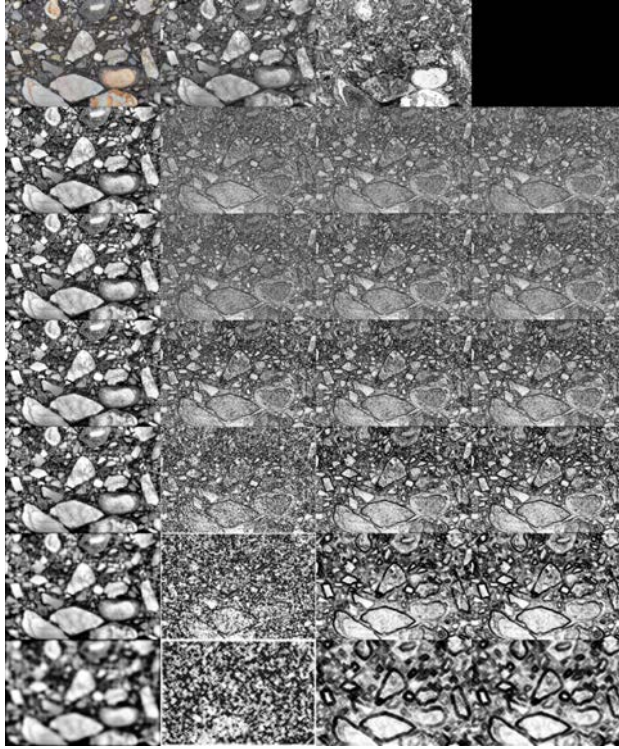

FIG. 4. Discriminating features. In the first row is the original image, its gray version and its color code. The following six rows have four columns that correspond to the mean, the entropy, the range and the standard deviation in the scales 5×5, 9×9, 17×17, 33×33, 65×65, and 129×129.

Looking at Fig. 4, it becomes evident that the M features are highly redundant, so they can be compressed into a smaller set of characteristics. Indeed, computing the covariance matrix between all the pixels of an image,

$$(3.14) \qquad C = \frac{1}{N_p - 1} \sum_{(x,y) \in \mathbb{Z}_{N_V} \times \mathbb{Z}_{N_H}} (d(x, y) - \mu) \left(d(x, y) - \mu\right)^{\mathrm{T}} \in \mathbb{R}^{M \times M}$$

and considering the corresponding eigenvalues and eigenvectors,

$$(3.15) \qquad C \cdot u_i = \lambda_i \cdot u_i, \qquad i = 1, 2, ..., M,$$

we notice that only few eigenvalues have significant magnitudes, as shown in Fig. 5. In it, the eigenvalues of the covariance matrix for the 26 data are plotted
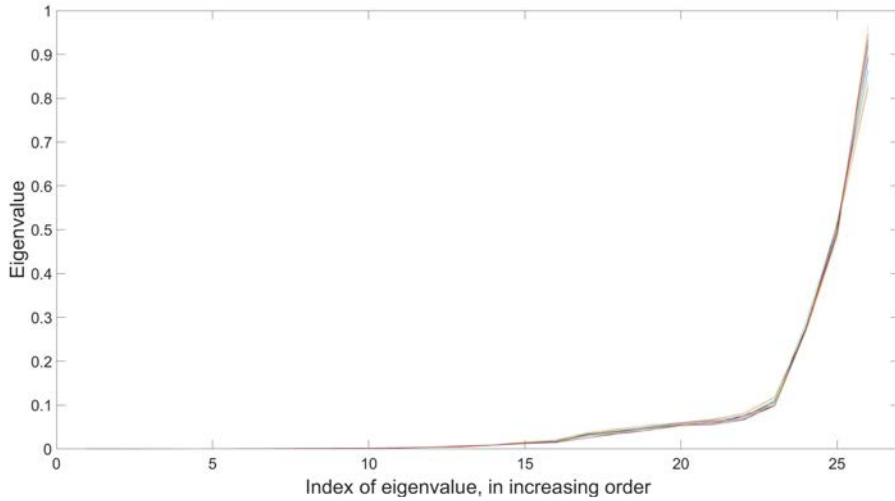
Fig. 5. Eigenvalues of the covariance matrix of 11 different images.

in all the pixels of 11 different images, where it can be seen that the correlation structure of the features is fundamentally independent of the image. Being a covariance matrix, C is positive definite and the eigenvectors form an orthogonal set on which we can project the 26 feature vectors, to obtain an orthogonal set of characteristics. We will use the projection on the eigenvectors corresponding to the eight major eigenvalues, as shown in Fig. 6. The eight components thus formed are known as the Principal Components of the features, $PC(x, y)$ [39].
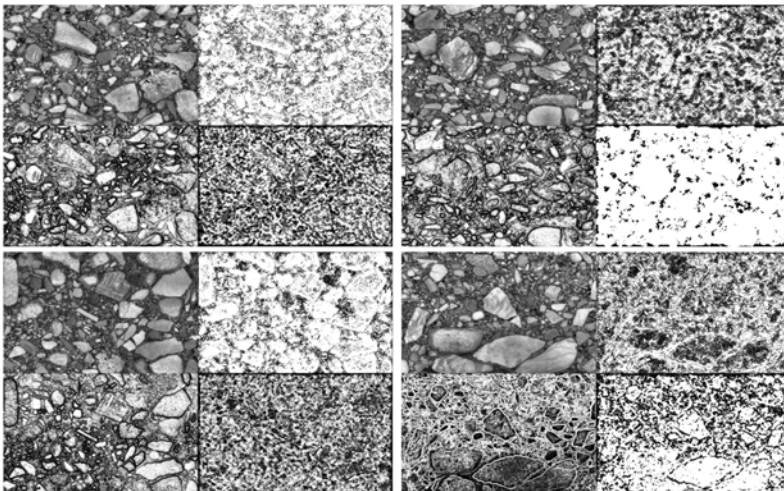
Fig. 6. Gray images and three principal components for four different photographs of asphalt mixtures.

By applying the two-means vector quantization technique on these eight principal components, slightly better results are obtained. This is essentially an extended Otsu's method.

To each pixel $(x, y) \in \mathbb{Z}_{NV} \times \mathbb{Z}_{NH}$ we have an 8-dimensional vector of principal components, $PC(x, y) \in \mathbb{R}^8$. We begin with two arbitrary vectors μ_g and μ_a for gravel and asphalt respectively. Then we assign each pixel of the image to the group that minimizes the distance to each level,

$$(3.16) \qquad I_S(x, y) = \begin{cases} 0 & \text{if } |PC(x, y) - \mu_a| < |PC(x, y) - \mu_g| \\[2mm] 1 & \text{if } |PC(x, y) - \mu_a| \geq |PC(x, y) - \mu_g| \end{cases}$$

$$\forall (x, y) \in \mathbb{Z}_{N_V} \times \mathbb{Z}_{N_H}.$$

Next we calculate the centroids of each region (the average values of the principal components of each of the two regions in which the image was divided),

$$(3.17)$$

$$\mu_g = \frac{\displaystyle\sum_{(x,y)\in\mathbb{Z}_{NV}\times\mathbb{Z}_{NH}} I_S(x, y) PC(x, y)}{\displaystyle\sum_{(u,v)\in\mathbb{Z}_{NV}\times\mathbb{Z}_{NH}} I_S(u, v)},$$

$$\mu_a = \frac{\displaystyle\sum_{(x,y)\in\mathbb{Z}_{NV}\times\mathbb{Z}_{NH}} (1 - I_S(x, y)) PC(x, y)}{\displaystyle\sum_{(u,v)\in\mathbb{Z}_{NV}\times\mathbb{Z}_{NH}} (1 - I_S(u, v))}.$$

Finally we iterate Eqs (3.16) and (3.17) until μ_g and μ_a converge to constant values. Again, we can run this algorithm over the whole image to get a global classification or we can use an adaptive approach working on smaller regions. Figure 7 compares both results.

For an additional standard classifier, we will consider a probabilistic model on the space of the $N = 8$ principal components. In particular, we will use the GMM model (Gaussian mixture model), estimating the parameters through the EM algorithm (Expectation/Maximization). The fundamental idea is to assume that the probability density function of the principal components of the pixel at any position (x, y) of the image domain has the following form:

$$(3.18) \qquad f\left(PC(x, y) \,|\, \mu_a, \Sigma_a, \mu_g, \Sigma_g, \alpha_g\right)$$

$$= \alpha_g f_g\left(PC(x, y) \,|\, \mu_g, \Sigma_g\right) + (1 - \alpha_g) f_a\left(PC(x, y) \,|\, \mu_a, \Sigma_a\right),$$
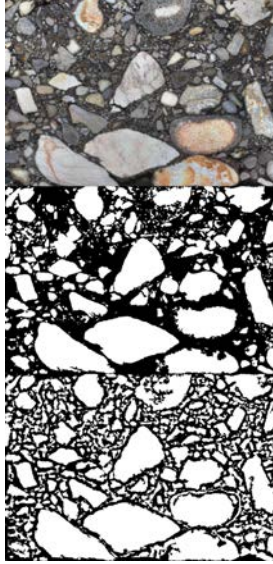
FIG. 7. Vector quantization with a global two-means algorithm and an adaptive
two-means algorithm over eight principal components.

where

$$0 \leq \alpha_g \leq 1,$$

$$f_g\left(PC(x,y)\,|\,\mu_g, \Sigma_g\right) = \frac{1}{\sqrt{(2\pi)^N \, |\Sigma_g|}}$$

(3.19)
$$\cdot \exp\left(-\frac{1}{2}\left(PC(x,y) - \mu_g\right)^{\mathrm{T}} \Sigma_g^{-1} \left(PC(x,y) - \mu_g\right)\right),$$

$$f_a\left(PC(x,y)\,|\,\mu_a, \Sigma_a\right) = \frac{1}{\sqrt{(2\pi)^N \, |\Sigma_a|}}$$

$$\cdot \exp\left(-\frac{1}{2}\left(PC(x,y) - \mu_a\right)^{\mathrm{T}} \Sigma_a^{-1} \left(PC(x,y) - \mu_a\right)\right).$$

$PC(x,y)$, as mentioned earlier, is a vector in $\mathbb{R}^N$ that corresponds to the set of N principal components of the pixel in the position (x,y); μ_g and μ_a are vectors in $\mathbb{R}^N$ that correspond to the expected values of the principal components in the gravel and asphalt pixels, respectively. Σ_g and Σ_a are matrices in $\mathbb{R}^{N \times N}$ that correspond to the correlation matrices of the principal components for the asphalt and aggregate pixels, respectively. We will estimate μ_g, μ_a, Σ_g, Σ_a, and a_g through the EM algorithm (Expectation/Maximization):

0. *Initialization*: From the segmented image I_S obtained with the adaptive Otsu's method or the adaptive vector-quantization method, we estimate the parameters of the distribution (3.18):

$$\alpha_g = \frac{1}{N_P} \sum_{(x,y)} I_S(x,y),$$

$$\mu_g = \frac{1}{N_P \cdot \alpha_g} \sum_{(x,y)} I_S(x,y) PC(xy),$$

$$(3.20) \quad \mu_a = \frac{1}{N_P \cdot (1-\alpha_g)} \sum_{(x,y)} (1-I_S(x,y))\, PC(xy),$$

$$\Sigma_g = \frac{1}{N_P \cdot \alpha_g} \sum_{(x,y)} (PC(x,y) - \mu_g) \cdot (PC(x,y) - \mu_g)^{\mathrm{T}} \cdot I_S(x,y),$$

$$\Sigma_a = \frac{1}{N_P \cdot (1-\alpha_g)} \sum_{(x,y)} (PC(x,y) - \mu_a) \cdot (PC(x,y) - \mu_a)^{\mathrm{T}} (1 - I_S(x,y)),$$

where N_P is the total number of pixels in the image.

1. *Expectation*: Based on the current estimates of μ_g, μ_a, Σ_g, Σ_a, and a_g, we compute the probability that each pixel is gravel using Bayes' rule:

$$(3.21) \quad P\left(G|\, PC(x,y)\right) = \frac{\alpha_g f_g\left(PC(x,y)\,|\mu_g, \Sigma_g\right)}{f^*},$$

where $f^* = \alpha_g f_g\left(PC(x,y)\,|\mu_g, \Sigma_g\right) + (1 - \alpha_g) f_a\left(PC(x,y)\,|\mu_a, \Sigma_a\right)$.

2. *Maximization*: With the above probability we re-estimate the parameters that maximize the likelihood. In the case of a Gaussian mixture, the sample averages are the optimal values:

$$\alpha_g = \frac{1}{N_P} \sum_{(x,y)} P\left(G|\, PC(x,y)\right),$$

$$\mu_g = \frac{1}{N_P \cdot \alpha_g} \sum_{(x,y)} PC(x,y) P\left(G|\, PC(x,y)\right),$$

$$(3.22) \quad \mu_a = \frac{1}{N_P \cdot (1-\alpha_g)} \sum_{(x,y)} PC(x,y)\left(1 - P\left(G|\, PC(x,y)\right)\right),$$

$$\Sigma_g = \frac{1}{N_P \cdot \alpha_g} \sum_{(x,y)} (PC(x,y) - \mu_g) \cdot (PC(x,y) - \mu_g)^{\mathrm{T}} P\left(G|\, PC(x,y)\right),$$

$$\Sigma_a = \frac{1}{N_P \cdot (1 - \alpha_g)} \sum_{(x,y)} (PC(x,y) - \mu_a)$$
$$\cdot (PC(x,y) - \mu_a)^{\mathrm{T}} \left(1 - P\left(G|\, PC(x,y)\right)\right).$$

3. We repeat steps 1 and 2 until convergence.

Figure 8 shows $P(G|PC)$ after convergence, both in the global and adaptive local modes. In this case, the adaptive method does not produce better results than the centralized one.
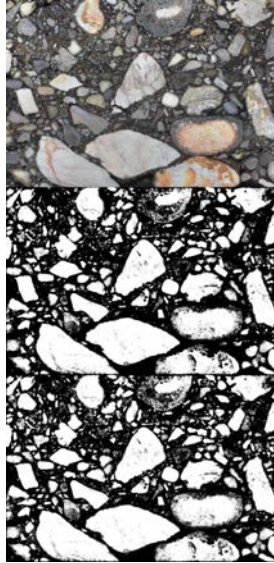

FIG. 8. Probability of each pixel being gravel given its 8 principal components, according to the GMM-EM model with a global algorithm and an adaptive local algorithm.

The logarithm of this probability is quantized (again through a multiclass Otsu method) to obtain a four classes segmentation image: A pixel with a value 3 is considered gravel, a pixel with a value 0 is considered asphalt, and a pixel with value 1 or 2 is considered in doubt (see Fig. 9).
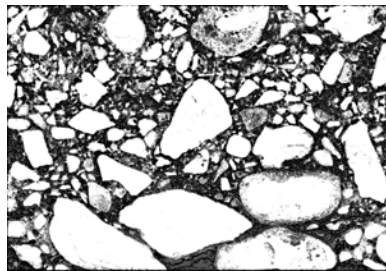
FIG. 9. Four-level quantization of the logarithm of the GMM-EM image of Fig. 8b.

3.2. Consensus among image processing methods through Cellular Automata

At this point we choose three plausible but imperfect segmentations of the image: I_1, I_2, and I_3, corresponding to the adaptive Otsu method (Fig. 3c),

the adaptive vector quantization method (Fig. 7c) and the quantized GMM-EM method (Fig. 9), respectively. We consider them as expert opinions that can be put together to obtain a better estimation. For example, when the three of them agree in a pixel to be asphalt or to be aggregate, we fix those pixels as correctly classified. For this purpose, we sum the normalized versions of the three images, $I = 3I_1 + 3I_2 + I_3$, as shown in Fig. 10 (recall I_1 and I_2 are binary images, with range $\mathbb{Z}_2$, and I_3 is a quaternary image, with range $\mathbb{Z}_4$). This way we obtain an image, I, quantized in 10 levels, from 0 to 9, according to the degree of coincidence among the three original images. The maximum value, 9, corresponds to those pixels where the three images agree in aggregate classification. The minimum value, 0, corresponds to those pixels where the three images agree in asphalt classification.
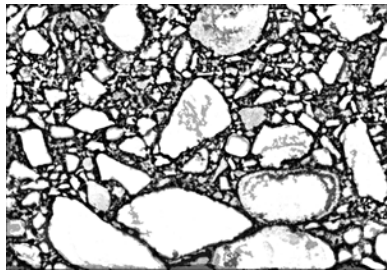

FIG. 10. Sum of the three images, for a total of ten classification levels.

Connected components with value 9 will be considered gravel. Connected components with value 0 will be considered asphalt. This is because the three methods agree on these classifications for those pixels. They will constitute seed images for a reconstruction process where intermediate pixels with values $0 < I(x, y) < 9$ will be incremented towards gravel or decremented towards asphalt, according to neighbor texture.

The first filter is obtained from two novel cellular automata (CA). A CA is a 4-tuple $\{I, S, N, F\}$, where I is a regular lattice of cells, S is the finite state of cells, N is the finite set of neighbors, and F is the function which assigns a new state to a cell according to the current state of its neighborhood, $F : S^{|N|} \rightarrow S$. In our case, I is the set of $N_V \times N_H$ pixels, $S = \{0, 1, ..., 9\}$ is the set of classification levels in I, N is a 3×3 neighborhood, and F is the following function:

$$(3.23) \qquad I(x, y) \leftarrow I(x, y) + \mathbf{1}_{(I(x,y)<m(x,y))} - \mathbf{1}_{(I(x,y)>m(x,y))},$$

where $m(x, y)$ is the mean of the pixels in a 3×3 neighborhood around (x, y) and $\mathbf{1}_A$ is the indicator function of statement A, with value 1 if A is true and value 0 if A is false. This rule, which tends to move the value of each pixel towards the mean of its neighborhoods, is applied to pixels between 1 and 8, since pixels that

have the values 0 or 9 are already classified as asphalt or aggregate, respectively, and they are no longer altered. The 3×3 neighborhood was chosen to solve for asphalt detection between different but closely located gravel units, so we had to sacrifice convergence speed in order to gain precision. Figure 11 shows some iterations of this first Cellular Automata.
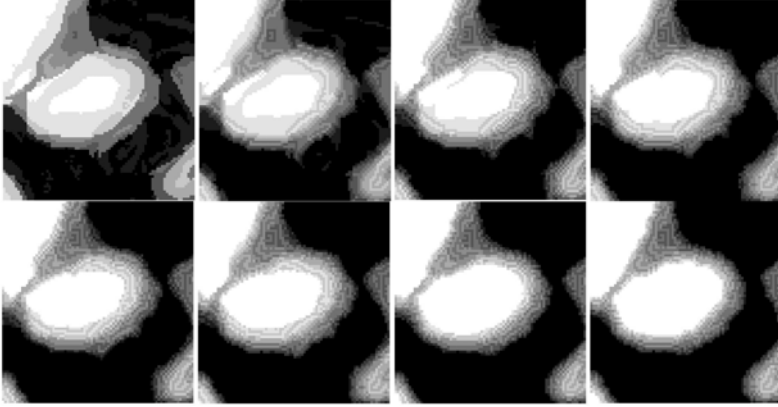

FIG. 11. Some iterations of the first cellular automata (3.23).

The pixels with value 0 in the output of the first cellular automaton are considered asphalt, as well as pixels with values 1 or 2 that are adjacent to pixels with value 0, according to this second CA:

$$(3.24) \qquad I(x,y) \leftarrow \begin{cases} 0 & \text{if } I(x,y) \in \{1,2\} \quad \text{and} \quad 0 \in N(x,y), \\ I(x,y) & \text{otherwise,} \end{cases}$$

where $N(x,y)$ is the 3×3 neighborhood around (x,y), as shown in Fig. 12.
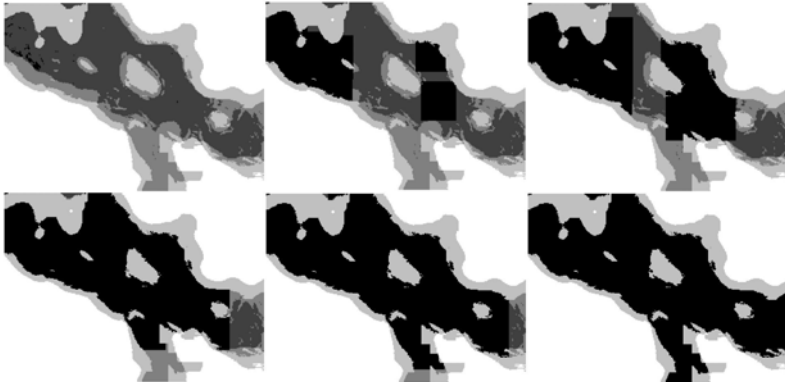

FIG. 12. Some iterations of the second cellular automata (3.24).

These two simple rules converge quickly toward a stable image or to a limit cycle, with highly reduced noise in both cases, as shown in Fig. 13.
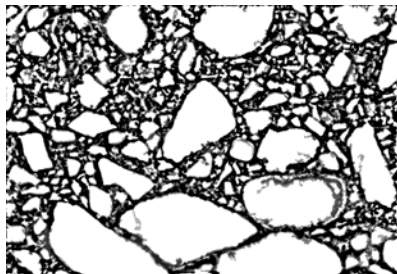

Fig. 13. Output of the cellular automata (3.23) and (3.24).

Then we find connected components with a gray value m between one and eight, whose border is composed of pixels with a gray value less than m. In principle, those connected components are also considered separated aggregate, since they are lighter than their surroundings. After filling holes on those regions, we label them and make them grow over darker areas with pixel values greater than 0, taking care not to merge separate regions, as shown in Fig. 14.
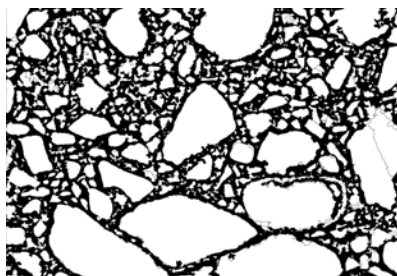

Fig. 14. Binary image with isolated regions.

Finally, adjacent regions are compared according to the distance between the mean of their principal components and the length of the common edge. Those regions that share a common long edge and are close according to the Euclidean distance between the means of the principal components are merged together as a single aggregate region. Similarly, objects with solidity smaller than 0.7 are separated into two different regions performing the same region growing process on two different seeds within the original single region. The final results for two of the available images are shown in Fig. 15.

We can notice, still, some wrongly merged regions and some wrongly separated regions, as well as some missed regions, although those problems occur
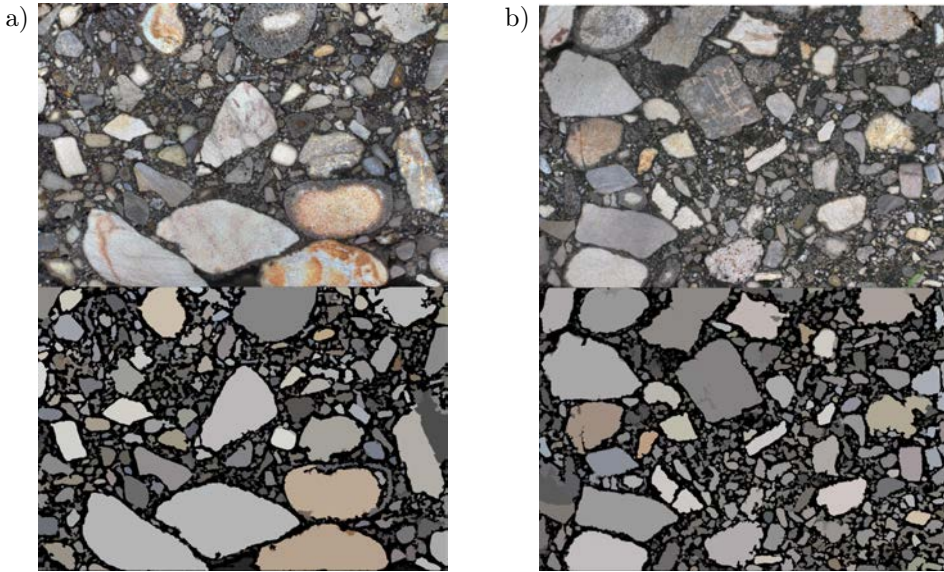
Fig. 15. Final segmentation of two images.

where, even for the human eye, segmentation decisions are hard to take. However, the resulting segmentation seems to be good enough for sieve size purposes, as will see in the following section.

4. Results

The validation of our image segmentation approach is gradation test of the pavement sample from the segmented image. In the laboratory, the material passes through a series of sieves that retain particles bigger than sieve mesh area. But in the specimen cut, the exposed area of each aggregate is just a random cut. We expect the aggregate areas in the image to be representative samples for the sieve filter in the original lab process. This way, the gradation test process is reduced to compute the fraction of total aggregate area due to those aggregate smaller than the given sieve mesh size.

Figure 16 shows the corresponding particle size distributions for three of the images. There, we compare the sieve size curve obtained by the image segmentation process with the sieve size curve used when the sample was manufactured. It can be seen that the curve represents accurately the aggregate composition of the pavement for sieve sizes greater than 100 microns, although they differ when the sieve size is less than 100 microns. The fraction of particles correctly classified by size, as compared to the sieving process of similar samples, is 90%.
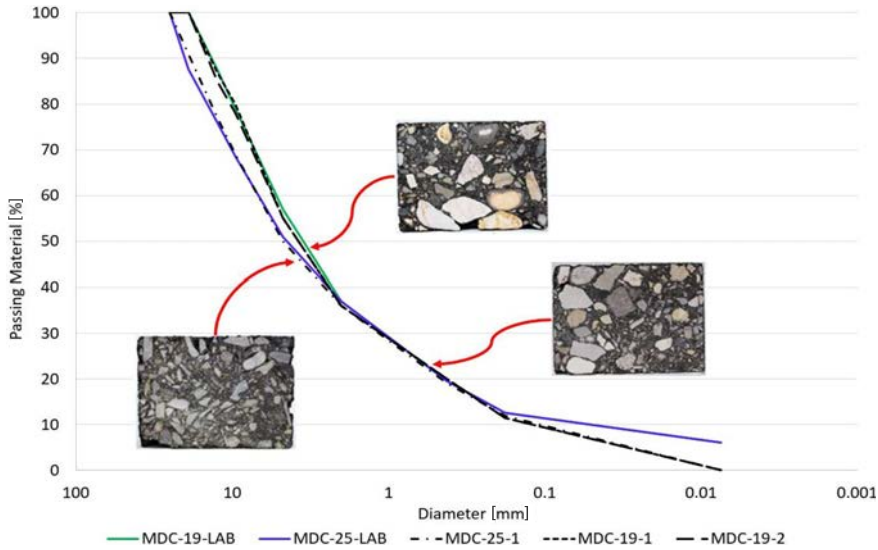
Fig. 16. Sieve size of three samples.

5. Conclusions

Digital image processing can be used for estimating the particle size distribution of aggregate in asphalt pavement. With this purposes, it is necessary to segment aggregate from asphalt accurately. In this paper, we described a segmentation procedure that includes the automatic detection of the sample region within the photographic picture. After a simple preprocessing based on adaptive histogram equalization and median filtering, we compute 26 discriminant features for each pixel and reduce redundancy among them through a principal component analysis that lead to a set of 8 final features. These features are used in three classical segmentation procedures: Adaptive Otsu, 2-means vector quantization, and a Gaussian mixture model estimated through the Expectation-Maximization method. None of these three methods are accurate enough for the purpose of this paper, so we combined them and process the resulting image using two cellular automata to get a much better segmentation image. Some additional morphological region growing and filtering are used to control over- and sub- segmentation. The results are comparable to those obtained through manual segmentation.

The final validation of the segmentation procedure is the estimation of different sieve size curves in pavement samples. In fact, we demonstrated that it is possible to perform the reconstruction of the laboratory curve from an image of the transverse section of the sample. One of the advantages of the method presented is that this process is done automatically. This allows having a versatile

tool that can be applied in quality control processes and as a verification tool in design methodologies. It should be noted that our method does not detect particles of size smaller than 100 microns.

As future work, the segmented images can be used to measure also shape, color and many other properties of the gravel for additional purposes like texture index, angularity, sphericity, form index, surface texture, among other characteristics that allows making a model of description of the mixture aggregate.

Acknowledgements

References

1. Zhang Y., Mohsen J.P., A project-based sustainability rating tool for pavement maintenance, *Engineering*, **4**(2): 200–208, 2018, doi: 10.1016/j.eng.2018.03.001.

2. Jamshidi A., Kurumisawa K., Nawa T., Jize M., White G., Performance of pavements incorporating industrial byproducts: A state-of-the-art study, *Journal of Cleaner Production*, **164**: 367–388, 2017, doi: 10.1016/j.jclepro.2017.06.223.

3. Gao L., Li H., Xie J., Yu Z., Charmot S., Evaluation of pavement performance for reclaimed asphalt materials in different layers, *Construction and Building Materials*, **159**: 561–566, 2018, doi: 10.1016/j.conbuildmat.2017.11.019.

4. Partl M.N. *et al.*, *Advances in Interlaboratory Testing and Evaluation of Bituminous Materials: State-of-the-Art Report of the RILEM Technical Committee 206-ATB*, Springer Netherlands, 2012.

5. Mataei B., Moghadas Nejad F., Zahedi M., Zakeri H., Evaluation of pavement surface drainage using an automated image acquisition and processing system, *Automation in Construction*, **86**: 240–255, 2018, doi: 10.1016/j.autcon.2017.11.010.

6. Wightman C., Muzzio F.J., Wilder J., A quantitative image analysis method for characterizing mixtures of granular materials, *Powder Technolog*, **86**(2): 165–176, 1996, doi:10.1016/S0032-5910(96)03178-6.

7. Reyes-Ortiz O.J., Mejía M., Useche-Castelblanco J.S., Image digital processing for the homogeneity calculation of an asphalt mix, *Congreso Internacional Multimedia*, Vol. 5, Universidad Militar, Bogotá, 2017.

8. Zhang K., Zhang Z., Luo Y., Huang S., Accurate detection and evaluation method for aggregate distribution uniformity of asphalt pavement, *Construction and Building Materials*, **152**: 715–730, 2017, doi: 10.1016/j.conbuildmat.2017.07.058.

9. Wu J., Wang L., Hou Y., Xiong H., Lu Y., Zhang L., A digital image analysis of gravel aggregate using CT scanning technique, *International Journal of Pavement Research and Technology*, **11**(2): 160–167, 2018, doi: 10.1016/j.ijprt.2017.08.002.

10. BONIFAZI G., PALMIERI R., SERRANTI S., Evaluation of attached mortar on recycled concrete aggregates by hyperspectral imaging, *Construction and Building Materials*, **169**: 835–842, 2018, doi: 10.1016/j.conbuildmat.2018.03.048.

11. GONZALEZ R.C., WOODS R.E., *Digital Image Processing* (3rd Ed.), Prentice-Hall, Inc., 2006.

12. OTSU N., A threshold selection method from Gray-Level histograms, *IEEE Transactions on Systems, Man, and Cybernetics*, **9**(1): 62–66, 1979, doi: 10.1109/TSMC.1979.4310076.

13. ZIOU D., TABBONE S., Edge detection techniques – an overview, *Pattern Recognition and Image Analysis: Advances in Mathematical Theory and Applications*, **8**(4): 537–559, 1998.

14. KAMBLE S.D., PAWAR D., JAGTAP S., Morphological image segmentation by morphological watersheds, *International Journal of Recent Scientific Research*, **10**(01): 30370–30374, 2019, doi: 10.24327/ijrsr.2019.1001.3045.

15. SHAPIRO L.G., STOCKMAN G., *Computer Vision*, New Jersey: Prentice Hall, 2001.

16. CHOUHAN S.S., KAUL A., SINGH U.P., Image segmentation using computational intelligence techniques: review, *Archives of Computational Methods in Engineering*, **26**(3): 533–596, 2019, doi: 10.1007/s11831-018-9257-4.

17. YUE Z.Q., BEKKING W., MORIN I., Application of digital image processing to quantitative study of asphalt concrete microstructure, *Transportation Research Record*, **1492**: 53–60, 1995.

18. LEE J.R.J., SMITH M. L., SMITH L.N., MIDHA P.S., A mathematical morphology approach to image based 3D particle shape analysis, *Machine Vision and Applications*, **16**(5): 282–288, 2005, doi: 10.1007/s00138-005-0181-x.

19. ZELELEW H.M., Application of digital image processing techniques for asphalt concrete mixture images, [in:] *The 12th International Conference of International Association for Computer Methods and Advances in Geomechanics (IACMAG)*, pp. 119–124, 2008.

20. HU J., QIAN Z., LIU Y., XUE Y., Microstructural characteristics of asphalt concrete with different gradations by X-ray CT, *Journal of Wuhan University of Technology-Mater. Sci. Ed.*, **32**(3): 625–632, 2017, doi: 10.1007/s11595-017-1644-4.

21. ARAMBULA E., GARBOCZI E.J., MASAD E., KASSEM E., Numerical analysis of moisture vapor diffusion in asphalt mixtures using digital images, *Materials and Structures*, **43**(7): 897–911, 2010, doi: 10.1617/s11527-009-9554-3.

22. MOON K.H., FALCHETTO A.C., Microstructural investigation of Hot Mix Asphalt (HMA) mixtures using Digital Image Processing (DIP), *KSCE Journal of Civil Engineering*, **19**(6): 1727–1737, 2015, doi: 10.1007/s12205-01.

23. YANG J., CHEN S., An online detection system for aggregate sizes and shapes based on digital image processing, *Mineralogy and Petrology*, **111**(1): 135–144, 2017, doi: 10.1007/s00710-016-0458-y.

24. YAN L. *et al.*, A numerical method for analyzing the permeability of heterogeneous geomaterials based on digital image processing, *Journal of Zhejiang University-SCIENCE A*, **18**(2): 124–137, 2017, doi: 10.1631/jzus.A1500335.

25. ZAKERI H., NEJAD F.M., FAHIMIFAR A., Image based techniques for crack detection, classification and quantification in asphalt pavement: a review, *Archives of Computational Methods in Engineering*, **24**(4): 935–977, 2017, doi: 10.1007/s11831-016-9194-z.

26. Khattak M.J., Khattab A., Rizvi H.R., Das S., Bhuyan M.R., Imaged-based discrete element modeling of hot mix asphalt mixtures, *Materials and Structures*, **48**(8): 2417–2430, 2015, doi: 10.1617/s11527-014-0328-1.

27. Bahia H.U., Coenen A., Tabatabaee N., Mixture design and compaction, [in:] *Advances in Interlaboratory Testing and Evaluation of Bituminous Materials*, Partl M. *et al.* [Eds], Springer Netherlands, 2013.

28. Modified-Asphalt-Research-Center, iPas software, University of Wisconsin at Madison, 2018, [Online]. Available: https://uwmarc.wisc.edu/ipas-software-package.

29. Doll B., Ozer H., Rivera-Perez J.J., Al-Qadi I.L., Lambros J., Investigation of viscoelastic fracture fields in asphalt mixtures using digital image correlation, *International Journal of Fracture*, **205**(1): 37–56, 2017, doi: 10.1007/s10704-017-0180-8.

30. Buttlar W.G. *et al.*, Digital image correlation techniques to investigate strain fields and cracking phenomena in asphalt materials, *Materials and Structures*, **47**(8): 1373–1390, 2014, doi: 10.1617/s11527-014-0362-z.

31. Mei A., Manzo C., Bassani C., Salvatori R., Allegrini A., Bitumen removal determination on asphalt pavement using digital imaging processing and spectral analysis, *Open Journal of Applied Sciences*, **4**(6): 366–374, 2014, doi: 10.4236/ojapps.2014.46034.

32. Sefidmazgi N.R., Tashman L., Bahia H., Internal structure characterization of asphalt mixtures for rutting performance using imaging analysis, *Road Materials and Pavement Design*, **13**(Sup1): 21–37, 2012, doi: 10.1080/14680629.2012.657045.